FT-NIR and DSC characterisation of water in opal

Paul Thomas[1], Boris Chauviré[1,2], Katharine Flower-Donaldson[1], Laurie Aldridge[3], Anthony Smallwood[1], Barry Liu[1]

[1]School of Mathematical and Physical Sciences, University of Technology Sydney, Sydney, Australia

[2]CNRS-UMR 5275, ISTerre, Université Grenoble Alpes, CS 40700, 38058 GRENOBLE Cedex 9.

[3]Australian Centre for Infrastructure Durability (ACID), Institute for Frontier Materials, Deakin University, Burwood, VIC, Australia

Abstract

Opal is a hydrous silica ($SiO_2.nH_2O$) formed through a dissolution-precipitation process. The formation process incorporates water into the structure as bound silanol and molecular water. As the water is distributed in a range of states, multiple methods of characterisation are required to identify each state. This study reports the results of temperature dependent FT-NIR and DSC investigation on natural opal samples of the opal-A (amorphous) and opal-CT (poorly crystalline cristobalite with tridymitic stacking faults) types. Significant differences in the melting behaviour of crystallisable water as well as differences in the spectral characteristics of the non-crystallisable molecular water are observed. These differences are ascribed to the different microstructures of the opal types.

Key Words

Opal-A, opal-CT, water, silica, FT-NIR, DSC

Introduction

Opal is a hydrous silica ($SiO_2.nH_2O$) which is formed through the aqueous dissolution of the silicate crust followed by the precipitation of opaline silica [1-3]. The dissolution-precipitation process results in a range of structural morphologies that have been described as; opal-A, amorphous opal; opal-CT, poorly crystalline cristobalite with tridymitic stacking faults; opal-C, a more highly ordered form of cristobalite, and; chalcedony, a microfibrous crystalline quartz [4-6]. The formation of each species is dependent on the solubility of the species being precipitated and the concentration of silica in solution, thus, the most amorphous silica species is transformed into more crystalline species following the Ostwald stepwise process [4, 7, 8]:

Silica source $\longrightarrow$ Opal-A $\longrightarrow$ Opal-CT $\longrightarrow$ Opal-C $\longrightarrow$ Chalcedony

The precipitation process is driven by the thermodynamic stability of the precipitating phase, but the phase produced is controlled by the kinetics of the precipitation, hence, the stepwise precipitation process is followed [8, 9]. This precipitation process is responsible for the different morphologies and microstructures of each type and how water is incorporated into the opal. This study will focus on the opal-A and -CT forms as these forms fit the types of opal that are currently mined for their characteristic play-of-colour.

The dissolution-precipitation process in aqueous media results in the confinement of water in the silica network and microstructure. As a result, water is present in opal as chemically bound silanol (Si-OH) functionalities and as molecular water [10-16]. The silanol species are found in internal surfaces such as capillary pores and voids as well as being distributed through the bulk phase as isolated silanol functionalities [10, 13]. Similarly, the molecular water exists in capillary pores and voids, as surface

adsorbed molecular water and as molecular water distributed through the cage or network structure of the silica.

The characterisation of these water types in opal has been carried out using a range of analytical methods. Near infrared (NIR) spectroscopy has been applied to the characterisation of both silanol and molecular water and the influence of hydrogen bonding on these species [10, 13, 15, 16]; NMR spectroscopy has been applied to the determination of the relative proportion of silanol functionalities in opal-A and -CT [17-21] and a range of thermal methods have been applied in the characterisation of opal and water in opal [5, 11-13, 21-29].

The characterisation of the states of water in opal is important for the understanding of gem quality opal, in particular, its origins of formation and its subsequent stability to whitening and crazing once the opal has been mined and processed as a gem [3, 12, 30]. Using DSC, for example, the confinement of water in opal-A and -CT, based on the melting behaviour of crystallisable water, has aided the characterisation of the microstructure through the estimation of the size and distribution of the water filled pores [12, 28, 29]. This study furthers the investigation of the states of water in opal-A and -CT specimens by investigating the melting behaviour of crystallisable water using DSC and temperature dependent NIR spectroscopy in the temperature range − 100 to + 30°C.

Materials and Methods

The six opal samples characterised in this study were sourced from opal traders and miners. The samples characterised are listed in Table 1. For FT-NIR analysis, samples of opal were cut into small pieces (circa 5 x 5 x 1 mm) with an Isomet low speed saw using deionised water as the cutting fluid. These samples were first characterised by XRD to identify the opal type. For DSC and TG analysis, circa 2 mm pieces were broken off the larger piece.

XRD was carried out using a Bruker Discovery D8 diffractometer set up in Bragg-Brentano configuration. Diffraction patterns were collected under ambient conditions between 5 and 50° 2θ with a step size of 0.04° using a Cu Ka radiation. Based on the diffraction patterns the opal samples were identified as either opal-A or -CT. The results of this classification are listed in Table 1.

FT-NIR was carried out using a Nicolet iS50 fitted with an NIR source and optics (tungsten-halogen white light source, CaF_2 beam splitter, InGaAs detector). Samples were placed on the hot stage of a Linkam LTS 420 accessory fitted with fused silica windows. The hot stage was loaded into the bench of the spectrometer in transmission mode. A liquid nitrogen reservoir produced a cold flow of nitrogen gas which was used to cool the assembly as well as provide a dry nitrogen purge to prevent condensation on the windows. Spectra were collected from − 100 to + 30 °C at 10 or 5 °C intervals. The temperature was set and approached at a heating rate of 2 °Cmin^{-1} before allowing the sample to equilibrate for two minutes prior to collecting the spectra. Spectra were collected from 4000 to 8000 cm^{-1} at a resolution of 4 cm^{-1} and averaged over 64 scans. The water combination mode in the 4600 to 5400 cm^{-1} region was baseline corrected using a linear baseline for spectral comparison of the data. The baseline corrected data were used to calculate the centre of mass (CoM) of the peak.

DSC was carried out using a TA Instruments Q2000 fitted with an RCS90 cooling system calibrated using high purity hexadecane, indium, tin and zinc. Heat flow calibration was carried out using indium. Although calibration had been carried out, Milli Q® water enclosed in TZero hermetically sealed aluminium pans was used as a reference and was found to have a heat of melting of 322 Jg^{-1} (c.f. 334 Jg^{-1} listed in the Handbook

of Chemistry and Physics 60th Edition CRC Press). The measured value was used as the reference value for the determination of the proportion of crystallisable water present.

Pieces of opal (20 to 25 mg) were loaded into hermetically sealed TZero aluminium pans and cycled between + 20 and – 80 °C at a heating / cooling rate of 2 °Cmin^{-1} with a 10 min isotherm after each heating or cooling step. Each sample was cycled between + 20 and – 80 °C five times to identify the effect of freezing on the melting behaviour of the water in opal. No systematic variation in the crystallisation or melting process was observed for any of the samples, although variation was observed in peak area measurement and is included in Table 1 as % standard deviation. The peak areas were calculated using a weighted average baseline based on linear tangents to the DSC curve before and after the melting peak. Due to the difficulty in measuring the onset temperature of the melting endotherm for the opal samples, the melting endotherms were integrated and the degree of conversion was determined. The onset temperature was set as the temperature at which 10 % conversion was reached. A similar calculation was carried out for the pure water sample to use as the reference temperature for pore radius estimation. It should be noted that the onset temperature for pure water melting was measured as -0.2 °C based on conventional onset temperature measurement using the TA Instruments Universal Analysis software.

TG measurements were carried out using a Netzsch STA 449 F5 Jupiter configured in TG mode. Samples (circa 40 mg of pieces) were loaded in platinum pans and covered with a platinum lid containing a pin hole. The purpose of the platinum lid was to contain the opal specimens in the pans in case of explosive fracture. This explosive fracture, resulting in ejection of pieces of opal into the furnace, occasionally occurs particularly in the case of opal-CT specimens. Samples were equilibrated at 40°C in a flowing helium atmosphere (40 mLmin^{-1}) for 20 min before heating to 1000°C at a heating rate of 2°Cmin^{-1}. An empty pan was also run in order to determine the baseline of the instrument. Water content was determined based on the mass loss between 40 and 1000°C.

Results and Discussion

DSC Analysis

The DSC data for the six opal specimens and pure water are shown in Figure 1. As expected, pure water is observed to melt at 0°C with a sharp onset that is typical for pure substances. The opal specimens all show melting endotherms over a range of temperatures with onset temperatures below 0 °C. The onset temperatures were determined as the temperature at which 10% conversion was reached by integration of the melting endotherm and are listed in Table 1.

The observation of onset temperatures below 0°C suggests that the water is melting from confined pores [31-33]. The degree by which the melting temperature is depressed reflects the size of the capillary pores or voids which may be estimated based on the empirical equation from Ref [31]:

$$r(\text{nm}) = -\frac{19.082}{\Delta T_{onset} + 0.1207} + \delta_m \qquad (1)$$

where r is the pore radius in nm, ΔT_{onset} is the difference between the onset temperature of the melting peak and that of pure water and δ_m is the thickness of non-crystallisable layer of water molecules adsorbed at the pore surface which, for the current study, was taken to be 1.12 nm based on the empirical measurements on controlled pore silicas [31]. Equation 1 is an empirical equation determined by measuring the onset temperatures of melting in controlled pore glasses. The basis of the equation has its

origins in melt depression based on the Gibbs-Thompson equation for melt depression as an inverse function of crystallite radius and on the melt depression of a crystallised liquid confined in a capillary pore as described by the Kelvin equation [31].

The pore radii for the samples investigated in this study have been calculated using Equation 1 and are listed in Table 1. The values determined here are consistent with previous studies [12, 29]. The void or capillary water melting temperatures are lower for opal-CT than opal-A and, hence, the calculated pore sizes are correspondingly smaller for opal-CT than opal-A ranging from a radius of 1.6 nm for the Tintenbar Brown Potch opal to greater than 50 nm for the Coober Pedy Shell Patch opal. The melting of crystallisable water in the Tintenbar opal appears to be complete by – 5°C suggesting that crystallisable water is only contained in capillary pores. The Mexican Red opal is similar and, although its melting range extends to slightly higher temperature, melting appears to be complete by 0°C again suggesting that the crystallisable water is contained in capillary pores. The opal-A samples, on the other hand, have onset temperatures below pure water freezing suggesting that some of the crystallisable water is contained in capillary pores, but the melting extends above zero suggesting that much of the crystallisable water is contained in large pores or voids. The Coober Pedy Shell Patch sample exhibits the highest onset temperature suggesting that crystallisable water is only contained in very large pores (> 50 nm in radius). These observations are consistent with the results on previous investigations into the DSC characterisation of the melting of crystallisable water in opal and are characteristic of the microstructures of these opals [12, 29].

The peak areas of the melting endotherm were determined to estimate the amount of crystallisable water contained in each opal. Based on the total water content as determined by the mass loss at 1000°C using TG (Figure 2), the proportion of crystallisable water was estimated and is listed in Table 1 for each specimen. For this set of samples, the proportion of crystallisable water is mostly between 19 to 27 %, the Mexican opal being the exception containing circa 40 % crystallisable water. These values are consistent with the previously determined values for a range of opal-A and -CT specimens which range between 5 and 42 % [12, 29]. It should be noted that the amount of crystallisable water is not a function of the opal type.

The amount of crystallisable water determined for these opals suggests that there is a significant proportion of non-crystallisable water in opal. Opal contains less than 30 % of the total water as silanol water (opal-CT contains more silanol water than opal-A) [17] and, based on the data of this and previous studies, the maximum crystallisable water content is 42% of the total water and it is generally much less. The proportion of the non-crystallisable molecular water contained in opal in must, therefore, be greater the 28%. Generally, the remaining water is attributed as surface adsorbed water in the case of capillary water and isolated or clusters of water molecules distributed through the silica network [10, 12, 13].

FT-NIR Analysis

The FT-NIR spectra are shown in Figure 3 for spectra collected at + 25 and at – 80 °C. The spectra collected at + 25 °C (Figure 2(a)) are characteristic of the spectra of opal-A and opal-CT [10, 15, 16] and water at ambient temperature [34, 35]. Similar spectra of water contained in mesoporous silica [21, 36] and silica glasses [37, 38] have been reported. There are three absorbance regions in the spectra; 4200 to 4600 cm^{-1} corresponding to silanol (SiOH) O-H stretching and an Si-O-Si stretch combination mode ($v_{Si02} + v_{OH}$) [37], 4600 to 5400 cm^{-1} corresponding to a water bending and stretching combination mode ($v_2 + v_3$) and 5400 to 7300 cm^{-1} which is predominantly associated with water stretching combination ($v_1 + v_3$), but is also composed at the high frequency end of the peak of free silanol stretching overtone ($2v_{OH}$) [38-41]. The silanol peaks in the 4200 to 4600 cm^{-1} are observed to be more prominent in opal-A than in opal-CT [15]. Both opal-A and -CT have significant water combination mode peaks in the 4600 to 5400 cm^{-1} and 5400 to

7300 cm^{-1} regions. Although there is a silanol overtone mode ($2\nu_{OH}$) around 7330 cm^{-1}, it diminishes significantly in intensity with hydrogen bonding in the presence of water [38, 42] and is not observed in these spectra. These assignments are based on the most intense modes in each region as the combination and overtone spectra of water and silanol functionalities are complex and the position and intensity of the peaks are sensitive to the environment and degree of hydrogen bonding of the functionalities [35, 38, 43].

The water combination regions are known to be sensitive to opal type and have been used to discriminate between opal-A and -CT [10, 15, 16]. The opal-A spectra at + 25°C (top four spectra in Figure 3(a)) show definite splitting of both the water combination modes into two peaks, 5280 cm^{-1} and a shoulder at circa 5100 cm^{-1} and 7110 cm^{-1} with a shoulder around 6900 cm^{-1}, which indicate two general states of water that correspond to bulk-like water and cage or more isolated water molecules [10, 12, 29]. The opal-CT water combination modes in Figure 3(a) (Tintenbar Brown and Mexican Red opals) are more rounded and present a single broad peak centred on 5240 cm^{-1} and 6950 cm^{-1} indicating a greater degree of hydrogen bonding [35, 38, 43]. The water spectrum at 25°C, also included in Figure 3(a), shows both the combination modes as rounded peaks at 5205 and 6930 cm^{-1}. These peaks are relatively broad and at lower frequency which is characteristic of the significant degree of hydrogen bonding in bulk water.

As previously discussed, a proportion of the molecular water contained in the opal structure is crystallisable and freezes as the temperature is reduced. For the opal samples studied here, the crystallisable water is frozen below – 50 °C. Spectra at – 80 °C are included in Figure 3(b) to represent the frozen state for comparison with the ambient temperature spectra. It is apparent that freezing of pure water results in a significant shift in both the water combination modes to lower frequency, consistent with reported data [34, 35, 44, 45]. A similar shift in water combination modes is observed for both the opal-A and -CT specimens. As the crystallisable water is the only species affected by the frequency shift, the peaks associated with the non-crystallisable water are accentuated with reducing temperature as they remain relatively unchanged by the cooling process. For opal-A, relatively narrow peaks at 5255 cm^{-1} and 7110 cm^{-1} become distinct (top four spectra in Figure 3(b)) while, for the opal-CT specimens (the Tintenbar Brown and Mexico Red in Figure 3(b)), the shifted band near 5090 cm^{-1} exhibits a shoulder at 5255 cm^{-1} and a peak develops at 7110 cm^{-1}. As these peaks are at relatively high frequency, they correspond to water which has a lower degree of hydrogen bonding suggesting that these peaks are due to the water that is present either as isolated molecules or in small clusters distributed through the silica network. The relative proportions of these peaks suggest that opal-A contains a greater degree of this type of non-crystallisable water than opals-CT.

The silanol functionalities in opal are present either as isolated silanol functionalities in the silica network or as surface functionalities (in capillary pores and on the surface). As the intensity of these peaks is dependent of the degree of hydrogen bonding [38, 42], the presence of these peaks (in the region 4200 to 4600 cm^{-1}) in the opal-A specimens suggest that these are associated with silanol functionalities distributed through the silica network rather than at surfaces (top four spectra in Figure 3(a)). These functionalities are not expected to be influenced by the freezing of water and are relatively unaffected by the reduction in temperature (top four spectra in Figure 3(b)). For opal-CT an assessment is more difficult to make as the silanol combination peaks are weak due to hydrogen bonding and overlap with the broad intense water combination mode near 5100 cm^{-1} (Tintenbar Brown and Mexico Red spectra in both Figure 3(a) and (b)).

Baseline corrected spectra in the 4600 to 5400 cm^{-1} region are shown in Figure 4 for temperatures from – 100 to + 30°C for pure water, Tintenbar Brown and Mintabie Grey opals showing the shift towards higher frequency as the temperature is raised (shading represents change of temperature from dark – low temperature, to light – high temperature). For water (Figure 4(a)), a sudden shift is observed as melting

occurs at 0°C while, for both the opal specimens (Figures 4(b) and (c)), a transition region is observed. In order to follow the change in position of the water combination mode with increasing temperature, the centre of mass (CoM) of the peak was calculated and is plotted in Figure 5. The sharp melting transition is observed for the pure water sample, while for each of the opal samples a transition region for melting is observed. This is consistent with the DSC data plotted in Figure 1 where a melting region is also observed for all the opal samples whereas a sharp melting peak is observed for the pure water.

The CoM for the 4600 to 5400 cm^{-1} region represents an average of the all states of molecular water present (bulk water, surface adsorbed water and isolated cage water). For the pure water sample, the range of states is associated with the bulk environment. On freezing the water molecules form a tetrahedral coordination resulting in significant hydrogen bonding and a shift in the peak to lower frequency (a red shift) [34]. As the temperature is increased, a blue shift in the frequency occurs until melting whereupon a sharp and significant blue shift in the frequency is observed as the structural change takes place (Figure 5). Above the melting point, a steady blue shift occurs with increasing temperature. Given that the water in the opals is relatively pure (i.e. there are no other potential sites for hydrogen bonding e.g. electrolytes present in solution [46]), the pure water sample data presented in this study represents the limiting case for confined pore water crystallisation (i.e. the pure water sample represents pores of infinite size).

The CoMs for the 4600 to 5400 cm^{-1} region for the opal specimens are all greater than that of water throughout the temperature range studied (Figure 5). The higher frequency of the CoMs indicates that on average the molecular water is less hydrogen bonded in opal than in pure bulk water. As the frequency of the CoM for the opal-A is higher than opal-CT, the molecular water in opal-A is less hydrogen bonded, on average, than opal-CT. The temperature dependence of the CoMs can also be roughly separated into the behaviour for opal-A and opal-CT. The CoMs for opal-CT are at significantly lower frequency in the frozen state. This suggests a high proportion of crystallisable water in the opal-CT specimens. Previous DSC studies [12, 29] and the DSC data presented above for this set of samples demonstrates that the measurable proportion of crystallisable water is not a function of the type of opal. An alternative explanation of the difference in the CoMs for opal-A and -CT is that crystallisation of the crystallisable water has an influence on the structure and hydrogen bonding of the adsorbed 'non-crystallisable' surface layer of water. The size and shape of the pores then becomes important; opal-A has relatively large interstitial voids which have lower surface area to volume ratio than the relatively small capillary pores in opal-CT. Consequently, there is a greater proportion of surface adsorbed (capillary) water that can be affected by the crystallisation of water in opal-CT and, hence, the 'average' state results in a CoM at lower frequency.

The transition in CoM from the frozen state to the melt state again differentiates the opal-A and -CT specimens (Figure 5). The melting process for the opal-CT specimens occurs over a wide range of temperatures and melting appears to be complete below 0°C. For the opal-A samples the melting process appears to begin at higher temperature than opal-CT and appears complete at 0°C for the Andamooka Potch and the Lightning Ridge Honey or above 0°C for the Coober Pedy Shell Patch and Mintabie opals. These observations are consistent with the DSC data and the concept of melting depression as a function of capillary pore size.

At temperatures above melting, the CoM values again discriminate the type of opal (Figure 5). The CoM values for opal-CT (Tintenbar Brown and Mexico Red) are greater than that of water, but are less than those of the opal-A specimens (top four curves in Figure 5). This suggests that, for both opal-A and -CT, there is a significant proportion of water which has a reduced degree of hydrogen bonding resulting in a higher frequency for the CoM. Further, as opal-A has a higher frequency CoM than that of opal-CT, the

proportion of water molecules with reduced degree of hydrogen bonding is greater suggesting that opal-A has a greater degree of water distributed through the silica network trapped in silica cages.

Comparison of the NIR and DSC

Firstly, no correlation can be made between the proportion of crystallisable water (deduced by DSC (Figure 1, Table 1)) and the position of the NIR absorptions bands in the 4600 to 5400 cm^{-1}region (Figure 5) as the proportion of crystallisable water as determined from DSC measurements in opal is not a function of the opal type (-A or -CT). The position of the NIR peak does, however, appear to be a function of the opal type and, based on the calculated pore size, it is reasoned that the shift in the 5100 cm^{-1} peak is associated with the pore size and shape rather than the amount of crystallisable water present (although this must be a factor in the position of the peak as well, as, for example, the Mexican opal has small pores, but it also has the largest crystallisable water content and so a CoM tending towards that of pure water is expected). As discussed above, the pore size in the opal-A samples is larger as the pores are formed primarily from interstitial voids between stacking spheres whereas the pores in the opal-CT samples are predominantly capillary pores [12, 29]. The increase in the surface area to volume ratio from large interstitial voids to capillary pores increases the proportion of the non-crystallisable surface adsorbed layer. As the non-crystallisable surface adsorbed layer is likely to be significantly hydrogen bonded, the difference in the CoMs of the two opal types is likely to be due to predominance of this type of water in opal-CT. The higher frequency for the opal-A CoMs is consistent with a greater proportion of the non-crystallisable molecular water existing as isolated water molecules or water molecules present in small clusters distributed through the silica network (i.e. less hydrogen bonded states of water).

The melting ranges observed in the DSC (Figure 1) correlate well with the shift of the NIR data (Figure 5). In order to verify this correlation, the onset temperature of the shift in the NIR data in Figure 5 have been estimated and are compared with the onset temperatures of the melting peak in the DSC curves (Table 1). As both characterisation techniques follow the melting process, DSC through heat flow as the endothermic melting process occurs and NIR through a change in the environment of the vibrating modes as melting occurs, a relationship between the estimated onset of melting from the shift of the NIR data as a function of the onset of the DSC melting should be observed. This relationship is plotted in Figure 6 and shows excellent correlation; the slope is close to proportionality and the correlation coefficient (r^2 = 0.99) also suggests an excellent relationship between the NIR and DSC data. The proportionality constant is slightly greater than one which reflects either the error in the measurement or divergence from correlation or both; the non-zero offset reflects the differences in the measurement type. Although there appears to be a strong relationship between the NIR and the DSC data, it should be noted that the correlation is tentative due to the spacing of the measurements in the NIR data.

Inspection of the DSC heating curves for each of the opal-A specimens reveals that part of the melting peak in the DSC is above 0°C. This 'superheating' is normally ascribed to the relative position of the temperature measurement thermocouple and the method in which DSC data is collected and, hence, the above zero melting for the opal-A samples would typically be considered to be due the experimental process. However, the elevated melting temperature for the Coober Pedy and the Mintabie opal specimens is observed in the NIR data (Figure 5) suggesting that the elevated temperature melting may be a true representation of the melting processes occurring in these opals and that melting for the Mintabie and Coober Pedy opals is completed at + 5°C indicating the presence of a superheated ice. Such elevated melting temperatures have been reported for the melting of water in confined pores in mineral specimens [47, 48]. As the density of water increases on melting, the elevated melting temperature could be ascribed to a state in which the ice is contained under negative pressure or in a tensile state. This state might arise if

the voids are only partially filled to a state where the increase in volume on the freezing of water to ice fills the cavity. On melting, the vapour phase, which is in equilibrium with the liquid phase in the melt state, fails to nucleate resulting in a reduction in the pressure and, hence, the ice exists under negative pressure and melting is delayed to a temperature above 0°C [49]. Verification of this postulate is required, but independent correlation between the DSC data and the NIR data suggests that this may be a reasonable explanation of the observations.

Conclusions

The melting behaviour of water confined in pores in opal-A and -CT has been investigated using DSC and temperature dependent FT-NIR. Both techniques demonstrate the presence of crystallisable water in opal and that the melting behaviour is dependent on the opal type. The variation in melting behaviour in the DSC has been ascribed to the difference in the microstructure of the opal types (capillary pores in opal-CT, voids or large pores in opal-A). The DSC data also suggests that a significant portion of the molecular water in opal is non-crystallisable.

The NIR data suggests that a proportion of the non-crystallisable water has a lower degree of hydrogen bonding through the accentuation of a peaks at higher frequency. The higher frequency peaks are revealed as the freezing of the crystallisable water shifts the highly hydrogen bonded water peaks to lower frequency. The fact that the amount of crystallisable water is not a function of the opal type (-A or -CT) suggests that it is the microstructure that is responsible for the differences in the NIR spectra; opal-CT has a greater degree of hydrogen bonded non-crystallisable water in capillary pores while opal-A has a greater degree of molecular water distributed though the silica network. Finally, the ice contained in the voids or interstices in opal-A may be subject to superheating, although this is a tentative assessment of the observations.

The temperature dependence of the melting behaviour of water using the DSC and FT-NIR spectroscopy has aided the characterisation of states of water present in opal. Correlation of the data has helped to deconvolve the states of water present and coupling the melting behaviour observed in DSC and NIR, has provided further insight into the microstructure of these two types of opal. Further, the use of these complementary techniques has provided information about the non-crystallisable water present in these solution precipitated silicas demonstrating the potential of coupled techniques in materials characterisation.

Acknowledgment

References

1.   Iler, R.K., *The Occurrence, Dissolution, and Deposition of Silica*. 1979. 3-93.
2.   Liesegang, M. and R. Milke, *Australian sedimentary opal-A and its associated minerals: Implications for natural silica sphere formation.* American Mineralogist, 2014. **99**(7): p. 1488-1499.
3.   Chauviré, B., et al., *The Precious Opal Deposit At Wegel Tena, Ethiopia: FormationViaSuccessive Pedogenesis Events.* The Canadian Mineralogist, 2017. **55**(4): p. 701-723.
4.   Williams, L.A., G.A. Parks, and D.A. Crerar, *Silica Diagenesis, I. Solubility Controls.* Journal of Sedimentary Petrology, 1985. **55**(3): p. 301-311.
5.   Jones, J.B. and E.R. Segnit, *The nature of opal I. nomenclature and constituent phases.* Journal of the Geological Society of Australia, 1971. **18**(1): p. 57-68.

6. Jones, J.B. and E.R. Segnit, *Genesis of cristobalite and tridymite at low temperatures.* Journal of the Geological Society of Australia, 1972. **18**(4): p. 419-422.
7. Morse, J.W. and W.H. Casey, *Ostwald Processes and Mineral Paragenesis in Sediments.* American Journal of Science, 1988. **288**: p. 537-560.
8. Williams, L.A. and D.A. Crerar, *Silica Diagenesis, II. General Mechanisms.* Journal of Sedimentary Petrology, 1985. **55**(3): p. 312-321.
9. Landmesser, M., *Mobility by Metastability: Silica Transport and Accumulation at Low Temperatures.* Chemie der Erde, 1995. **55**: p. 149-176.
10. Langer, K. and O.W. Forke, *Near Infrared Spectra (4000-9000 cm-1) of Opals and the Role of "Water" in these SiO2.nH2O minerals.* 1974, 1974. **52**(1): p. 17-51.
11. Smallwood, A., et al., *Application of a Fickian model of diffusion to the dehydration of graded specimens of a precious Australian sedimentary opal derived from Coober Pedy.* Journal of Thermal Analysis and Calorimetry, 2009. **97**(2): p. 685-688.
12. Chauviré, B. and P.S. Thomas, *DSC of natural opal: insights into the incorporation of crystallisable water in the opal microstructure.* Journal of Thermal Analysis and Calorimetry, 2019.
13. Thomas, P.S., K. Heide, and M. Földvari, *Water and hydrogen release from perlites and opal.* Journal of Thermal Analysis and Calorimetry, 2014. **120**(1): p. 95-101.
14. Day, R. and B. Jones, *Variations in Water Content in Opal-A and Opal-CT from Geyser Discharge Aprons.* Journal of Sedimentary Research, 2008. **78**(4): p. 301-315.
15. Chauviré, B., B. Rondeau, and N. Mangold, *Near infrared signature of opal and chalcedony as a proxy for their structure and formation conditions.* European Journal of Mineralogy, 2017. **29**(3): p. 409-421.
16. Boboň, M., et al., *State of water molecules and silanol groups in opal minerals: a near infrared spectroscopic study of opals from Slovakia.* Physics and Chemistry of Minerals, 2011. **38**(10): p. 809-818.
17. Brown, L.D., A.S. Ray, and P.S. Thomas, *29Si and 27Al NMR study of amorphous and paracrystalline opals from Australia.* Journal of Non-Crystalline Solids, 2003. **332**(1-3): p. 242-248.
18. Graetsch, H., H. Gies, and I. Topalovic, *NMR, XRD, IR Study on Microcrystalline Opals.* Physics and Chemistry of Minerals, 1994. **21**: p. 166-175.
19. Adams, S.J., G.E. Hawkes, and E.H. Curzon, *Solid State 29Si nuclear Magnetic Resonance Study of Opals and other Hydrous Silicas.* American Mineralogist, 1991. **76**: p. 1863-1871.
20. Chemtob, S.M., G.R. Rossman, and J.F. Stebbins, *Natural hydrous amorphous silica: Quantitation of network speciation and hydroxyl content by 29Si MAS NMR and vibrational spectroscopy.* American Mineralogist, 2012. **97**(1): p. 203-211.
21. Gallas, J.P., et al., *Quantification of water and silanol species on various silicas by coupling IR spectroscopy and in-situ thermogravimetry.* Langmuir, 2009. **25**(10): p. 5825-34.
22. Thomas, P.S., et al., *Thermal properties of Australian sedimentary opals and Czech moldavites.* Journal of Thermal Analysis and Calorimetry, 2010. **99**(3): p. 861-867.
23. Brown, L.D., et al., *Thermal Characteristics of Australian Sedimentary Opals.* Journal of Thermal Analysis and Calorimetry, 2002. **68**: p. 31-36.
24. Smallwood, A., P.S. Thomas, and A.S. Ray, *Characterisation of the Dehydration Behaviour of Australian Sedimentary and Volcanic Precious Opal by Thermal Methods.* Journal of Thermal Analysis and Calorimetry, 2008. **92**: p. 91-95.
25. Smallwood, A., P.S. Thomas, and A.S. Ray. *Thermophysical Properties of Australian Opal.* in *Nineth International Congress for Applied Mineralogy.* 2008. Brisbane: Australian Institute of Mining and Mineralogy Publication
26. Smallwood, A., et al., *TMA and SEM Characterisation of the Thermal Dehydration of Australian Sedimentary Opal.* Journal of Thermal Analysis and Calorimetry, 2007. **88**: p. 185-188.
27. Thomas, P., et al., *Thermophysical Properties of Natural Glasses at the Extremes of the Thermal History Profile.* 2011. **8**: p. 311-325.
28. Thomas, P.S., L. Aldridge, and A. Smallwood, *Water in Opal - What Can It Tell Us?* InColor, 2019. **41**: p. 62-69.
29. Thomas, P.S., J.-P. Guerbois, and A. Smallwood, *Low temperature DSC characterisation of water in opal.* Journal of Thermal Analysis and Calorimetry, 2013. **113**(3): p. 1255-1260.

30. Pearson, G., *Role of Water in Cracking of Opal.* Australian Gemmologist, 1985. **15**(12): p. 435-445.

31. Landry, M.R., *Thermoporometry by differential scanning calorimetry: experimental considerations and applications.* Thermochimica Acta, 2005. **433**(1-2): p. 27-50.

32. Ishikiriyama, K. and M. Todoki, *Pore Size Distribution Measurements of Silica Gels by Means of Differential Scanning Calorimetry II. Thermoporosity.* Journal of Colloid and Interface Science, 1995. **171**: p. 103-111.

33. Ishikiriyama, K., M. Todoki, and K. Motomura, *Pore Size Distribution (PSD) Measurements of Silica Gels by Means of Differential Scanning Calorimetry 1. Optimisation for Determination of PSD.* Journal of Colloid and Interface Science, 1995. **171**: p. 92-102.

34. Cupane, A., M. Levantino, and M.G. Santangelo, *Near Infrared Spectra of Water in Silica Hydrogels in the Temperature Interval 365-5 K.* Journal of Physical Chemistry B, 2002. **106**: p. 11323-11328.

35. Yamatera, H., B. Fitzpatric, and G. Gordon, *Near Infrared Spectra of Water and Aquous Solutions.* Journal of Molecular Spectroscopy, 1964. **14**: p. 268-278.

36. Anderson, J.H. and K.A. Wickersheim, *Near Infrared Characterisation of Water and Hydroxyl Groups on Silica Surfaces.* Surface Science, 1964. **2**: p. 252-260.

37. Stone, J. and G.E. Walrafen, *Overtone vibrations of OH groups in fused silica optical fibers.* The Journal of Chemical Physics, 1982. **76**(4): p. 1712-1722.

38. Litvan, G.G. and R.S. Yamasaki, *Simultaneous determination of the spectroscopic and adsorption isotherms of water on silica.* Materiaux et Constructions, 1972. **5**: p. 199-207.

39. Burneau, A., et al., *Comparative Study of the Surfac Hydroxyl Groups of Fumed and Precipitated Silica.* Langmuir, 1990. **6**: p. 1364-1372.

40. Burneau, A. and C.d. Carteret, *Near infrared and ab initio study of the vibrational modes of isolated silanol on silica.* Physical Chemistry Chemical Physics, 2000. **2**(14): p. 3217-3226.

41. Cannas, C., et al., *29Si CPMAS NMR and near-IR study of sol–gel microporous silica with tunable surface area.* Journal of Non-Crystalline Solids, 2005. **351**(43-45): p. 3476-3482.

42. Yamauchi, H. and S. Kondo, *The Structure of Water and Methanol Adsorbed on Silica Gel by FT-NIR Spectroscopy.* Colloid and Polymer Sciecne, 1988. **265**: p. 855-861.

43. Workman, J. and L. Weyer, *Practical Guide to Interpretive Near Infrared Spectroscopy*. 2008: CRC Press.

44. Grundy, W.M. and B. Schmitt, *The temperature-dependent near-infrared absorption spectrum of hexagonal H2O ice.* Journal of Geophysical Research: Planets, 1998. **103**(E11): p. 25809-25822.

45. Mastrapa, R., et al., *Optical constants of amorphous and crystalline H2O-ice in the near infrared from 1.1 to 2.6 µm.* Icarus, 2008. **197**(1): p. 307-320.

46. Koniorczyk, M. and D. Bednarska, *Kinetics of water freezing from inorganic salt solution confined in mesopores.* Thermochimica Acta, 2019. **682**.

47. Roedder, E., *Metastable Superheated Ice in Liquid-Water Inclusions Under High Negative Pressure.* Science, 1967. **155**: p. 1413-1416.

48. Henderson, S.J. and R.J. Speedy, *Melting Temperature of Ice at Positive and Negative Pressures.* Journal of Physical Chemistry, 1987. **91**: p. 3069-3072.

49. Kamb, B., *Superheated Ice.* Science, 1970. **169**: p. 1343-1344.

List of Tables

Table 1.

Characterisation details of the opal samples investigated; opal type was based on XRD pattern, crystallisable water peak area was determined from a weighted averaged baseline corrected melting peak, the water content was determined from the mass loss at 1000°C, % crystallisable water was determined from the equivalent heat of melting for Milli Q® water enclosed in TZero hermetically sealed pans, the DSC onset temperature was determined as the temperature at which 10 % conversion was observed, the pore radius was determined from the DSC onset temperature, and the NIR onset temperature was estimated from the data in Figure 5.

List of Figures

Figure 1

DSC curves for samples of opal heated from – 80 to + 20 °C. Curves have been shifted for clarity. The scale is 0.05 W/g between tick marks for the opal samples and 5 W/g between tick marks for water. Onset for water melting is at – 0.2°C. The baselines used in calculating the melting peak areas have also been plotted.

Figure 2

TG % mass change data plotted as a function of temperature for the opal samples: (a) Andamooka Potch, (b) Mintabie Grey POC, (c) Lightning Ridge Honey Potch, (d) Coober Pedy Shell Patch POC, (e) Tintenbar Brown Potch and (f) Mexico Red.

Figure 3

Transmittance spectra for opal samples and water for spectra collected at (a) + 25°C and (b) – 80°C.

Figure 4

Overlay of spectra of (a) water, (b) Tintenbar Brown Potch opal and (c) Mintabie Grey POC opal collected from – 100 (darkest) to + 30°C (lightest).

Figure 5

Plot of the centre of mass of the 5100 cm^{-1} combination mode as a function of temperature for the samples studied and listed in Table 1. For comparison, the melting of water is included.

Figure 6

Plot of the onset of melting based on the FT-NIR data as a function of the onset of melting peak in the DSC. Error bars in the NIR data reflect the separation of points at onset temperature.

Table 1.

Characterisation details of the opal samples investigated; opal type was based on XRD pattern, crystallisable water peak area was determined from a weighted averaged baseline corrected melting peak, the water content was determined from the mass loss at 1000°C, % crystallisable water was determined from the equivalent heat of melting for Milli Q® water enclosed in TZero hermetically sealed pans, the DSC onset temperature was determined as the temperature at which 10 % conversion was observed, the pore radius was determined from the DSC onset temperature, and the NIR onset temperature was estimated from the data in Figure 5.

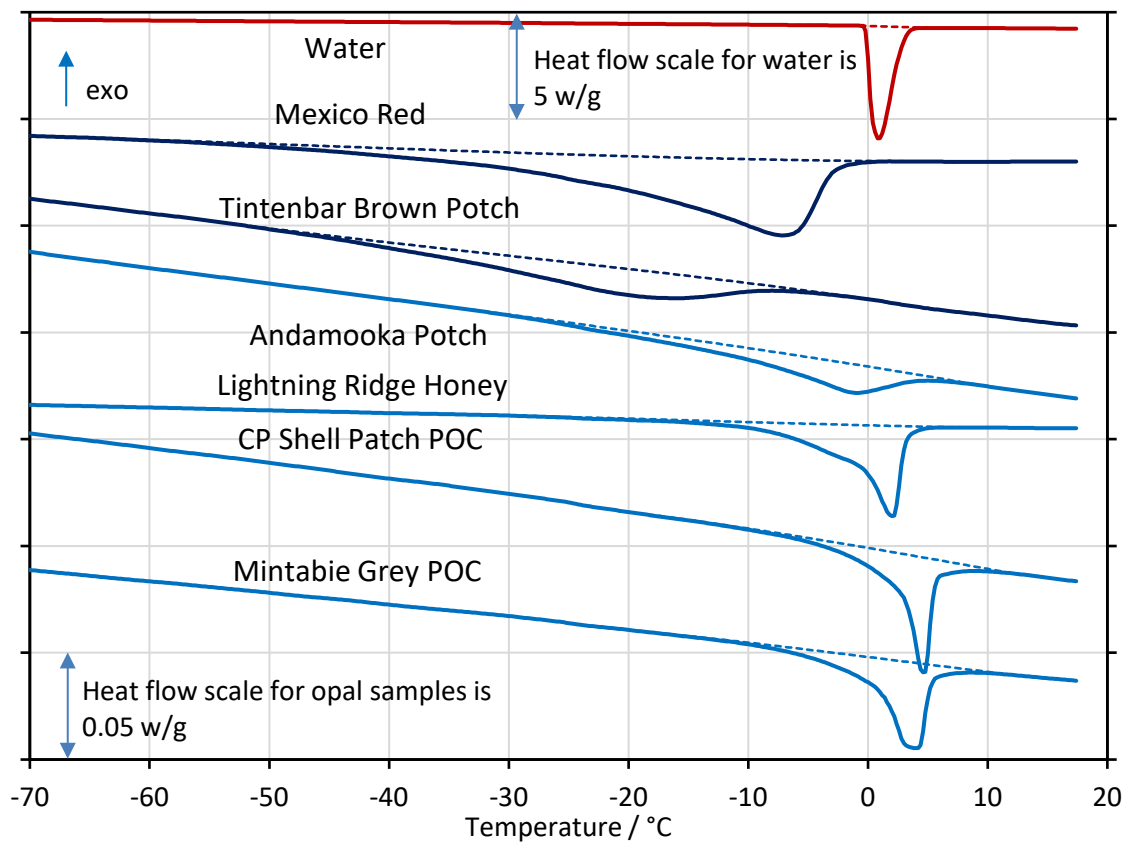| Sample	Opal Type	Crystallisable Water Peak Area / J/g	Total Water Content / %	% Crystallisable Water	DSC Onset Temp. / °C	DSC Onset Pore Radius / nm	NIR Onset Temp. / °C
Andamooka Grey / Honey Potch (A2)	A	-4.3 ± 0.4	6.4 ± 0.2	20.9 ± 2.0	-15.9 ± 0.7	2.3	-19.7
Lightning Ridge Honey Potch (LR1)	A	-6.9 ± 0.2	8.1 ± 0.2	26.6 ± 1.1	-8.9 ± 0.9	3.2	-9.1
Coober Pedy Shell Patch	A	-4.7 ± 0.2	7.5 ± 0.2	19.3 ± 1.0	-0.2 ± 0.2	51	-1.4
Mintabie Grey POC	A	-5.2 ± 0.1	6.6 ± 0.2	24.5 ± 0.9	-2.0 ± 0.1	9.9	-3.2
Mexican Red (Fire Opal)	CT	-17.5 ± 0.8	13.4 ± 0.4	40.7 ± 2.2	-30.7 ± 1.4	1.7	-33.8
Tintenbar Brown Potch (TBR1)	CT	-6.6 ± 0.5	9.7 ± 0.3	21.2 ± 1.7	-36.5 ± 2.7	1.6	-44.9
Milli Q® Water	-	-322.4 ± 1	-	-	0.3 ± 0.01	-	-

Figure 1

DSC curves for samples of opal heated from − 80 to + 20 °C. Curves have been shifted for clarity. The scale is 0.05 W/g between tick marks for the opal samples and 5 W/g between tick marks for water. Onset for water melting is at − 0.2°C. The baselines used in calculating the melting peak areas have also been plotted.
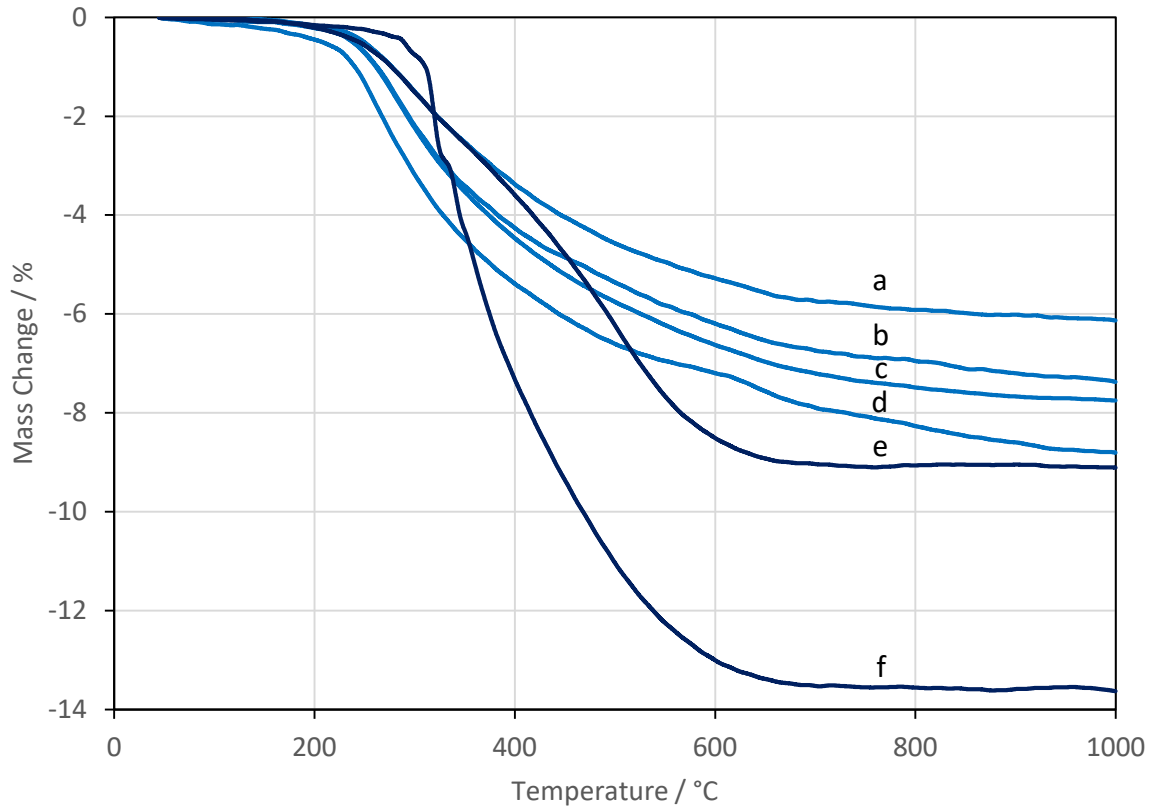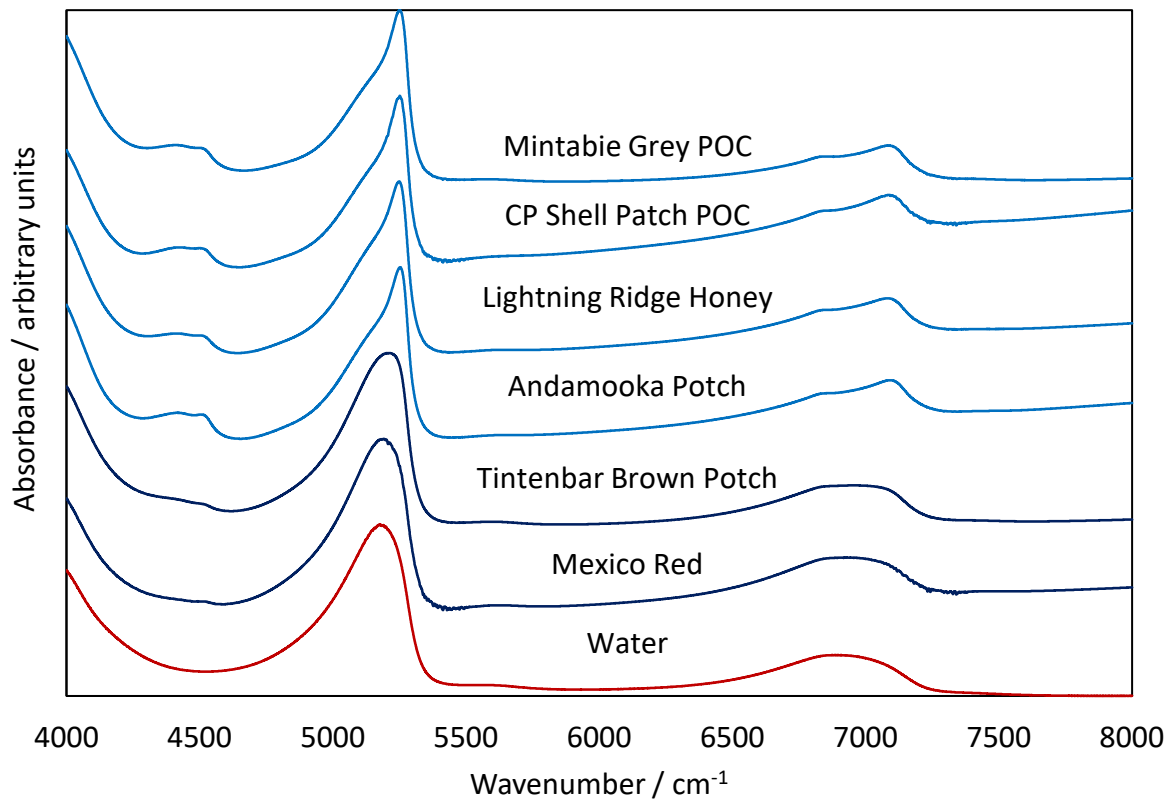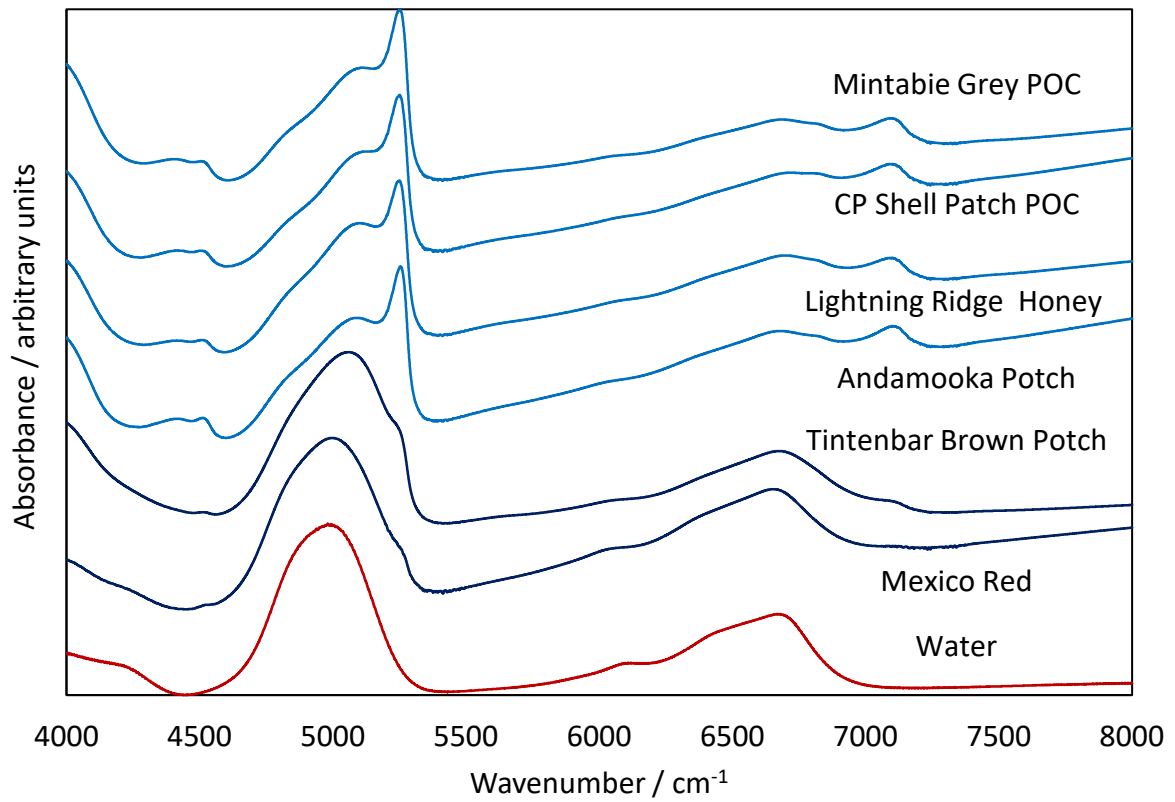
Figure 2

TG % mass change data plotted as a function of temperature for the opal samples: (a) Andamooka Potch, (b) Mintabie Grey POC, (c) Lightning Ridge Honey Potch, (d) Coober Pedy Shell Patch POC, (e) Tintenbar Brown Potch and (f) Mexico Red.
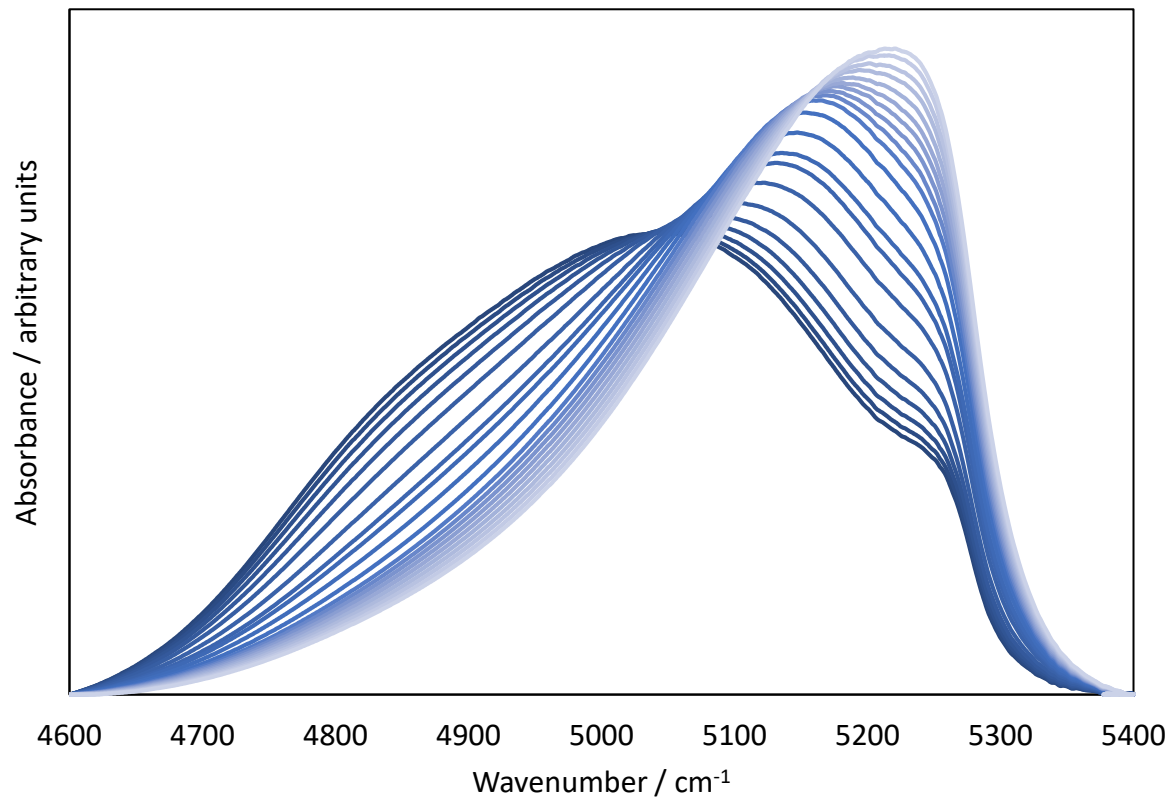
Mintabie Grey POC

CP Shell Patch POC

Lightning Ridge Honey

Andamooka Potch

Tintenbar Brown Potch

Mexico Red

Water

Absorbance / arbitrary units

4000   4500   5000   5500   6000   6500   7000   7500   8000

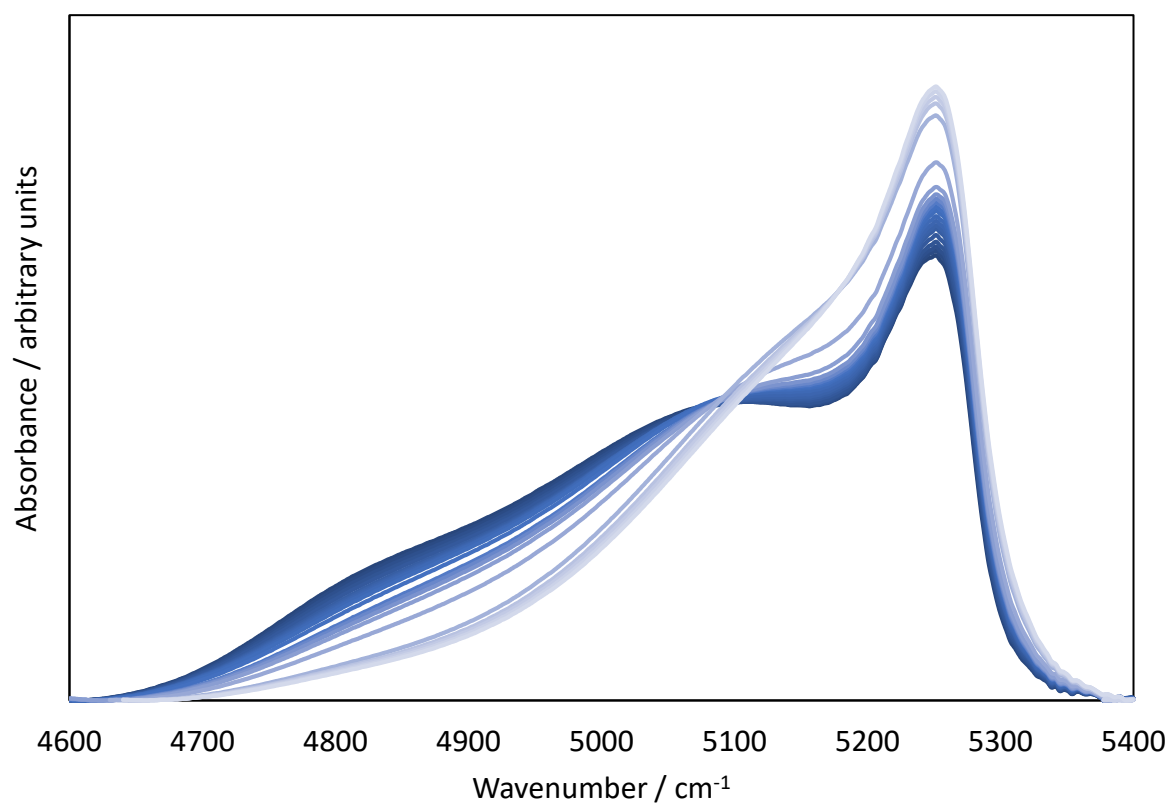Wavenumber / cm^{-1}

(a)

(b)

Figure 3

Transmittance spectra for opal samples and water for spectra collected at (a) + 25°C and (b) – 80°C.

(a)

(b)

(c)

Figure 4

Overlay of spectra of (a) water, (b) Tintenbar Brown Potch opal and (c) Mintabie Grey POC opal collected from − 100 (darkest) to + 30°C (lightest).
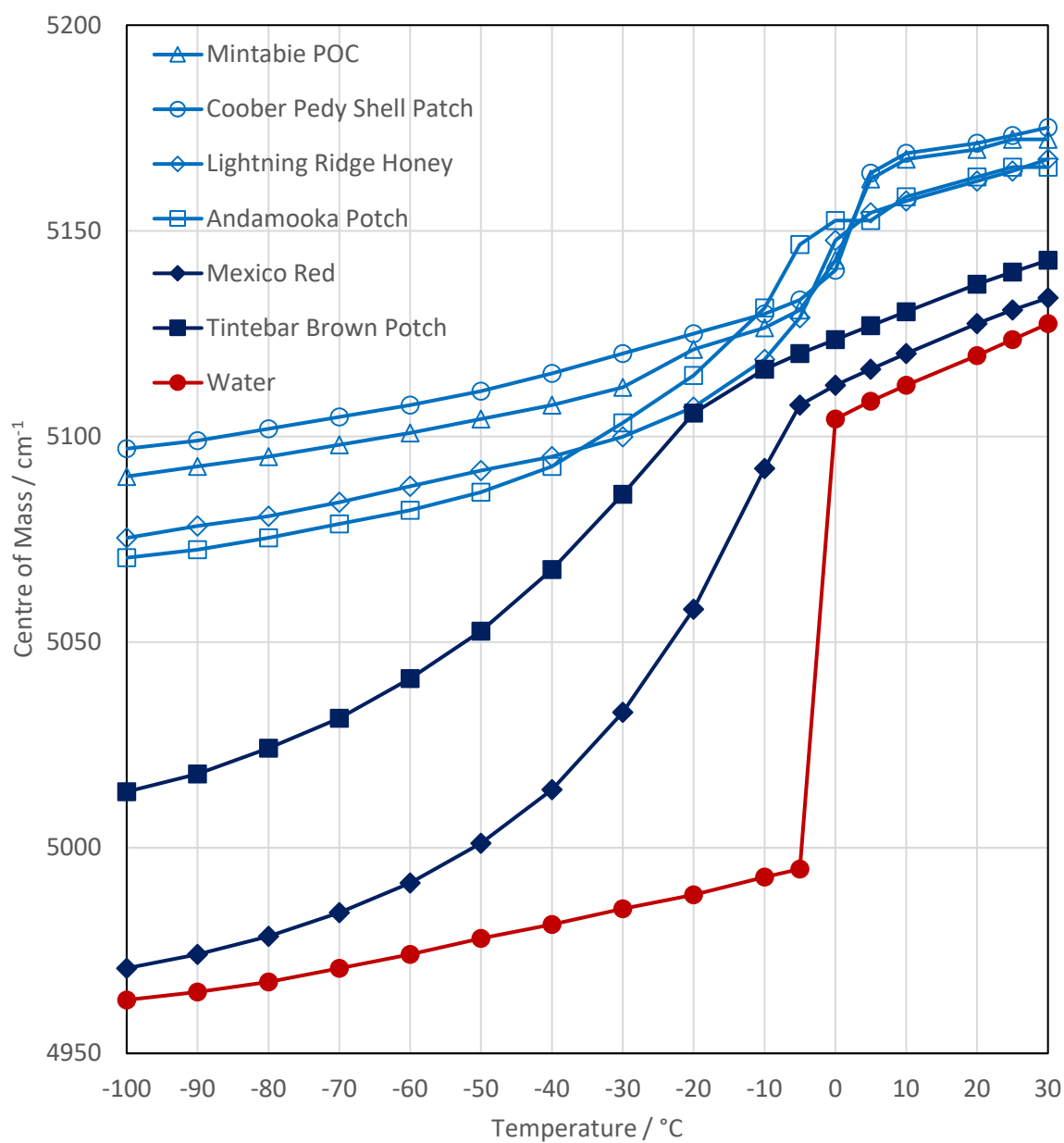
Figure 5

Plot of the centre of mass of the 5100 cm^{-1} combination mode as a function of temperature for the samples studied and listed in Table 1. For comparison, the melting of water is included.
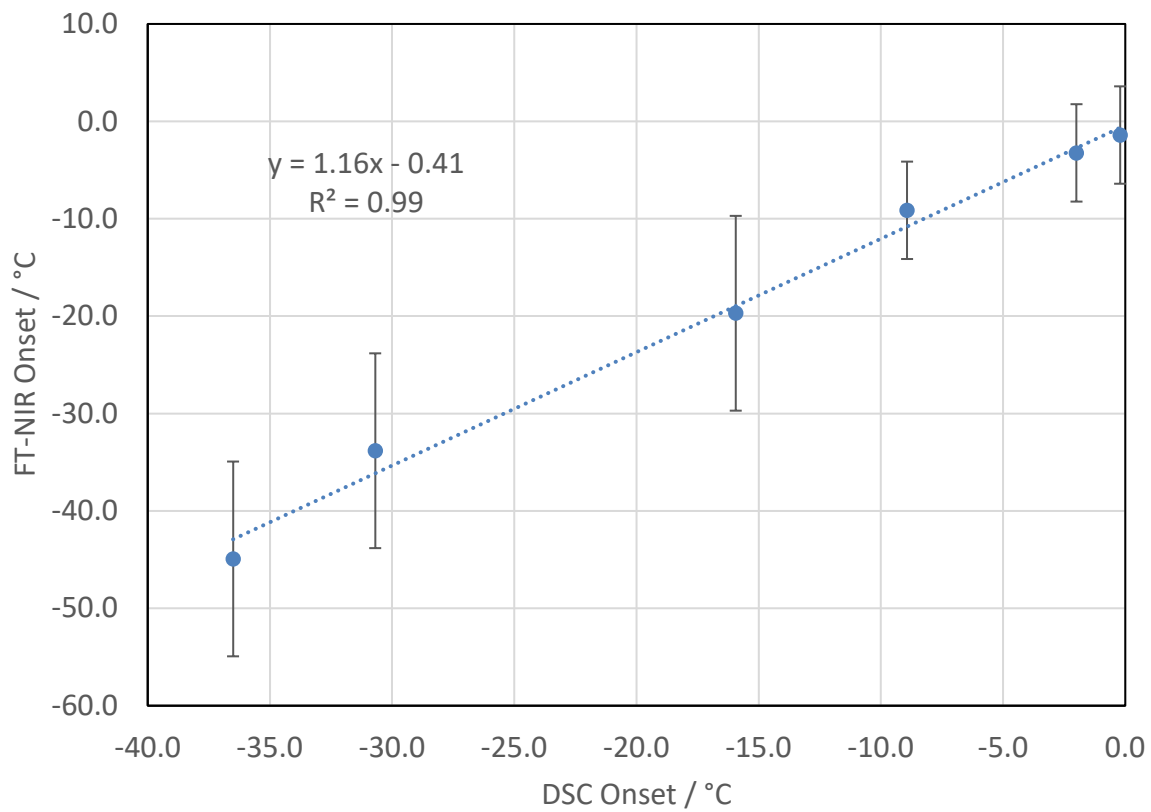
Figure 6

Plot of the onset of melting based on the FT-NIR data as a function of the onset of melting peak in the DSC. Error bars in the NIR data reflect the separation of points at onset temperature.